The Final Stages of Slip and Volcanism on an Oceanic Detachment Fault at 13°48'N, Mid-Atlantic Ridge

R. E. Parnell-Turner[1*], E. Mittelstaedt[2], M. D. Kurz[1], M. Jones[1], S. A. Soule[1], F. Klein[1], V. D. Wanless[3] and D. J. Fornari[1]

[1]Woods Hole Oceanographic Institution, 266 Woods Hole Road, Woods Hole, MA 02543, USA

[2]Department of Geological Sciences, University of Idaho, Moscow, ID 83844, USA

[3]Department of Geosciences, Boise State University, Boise, ID 83725, USA

*now at Institute of Geophysics and Planetary Physics, Scripps Institution of Oceanography, University of California, San Diego, La Jolla, CA, USA

Corresponding author: Ross Parnell-Turner (rparnellturner@ucsd.edu)

Key Points

- Autonomous underwater vehicle and submersible surveys of inactive oceanic detachment fault on Mid-Atlantic Ridge
- Sediment thickness and volatile content of lava used to track tectonic activity
- Seafloor observations suggest that slip continued after a volcanic intrusion into detachment fault footwall

Abstract

While processes associated with initiation and maintenance of oceanic detachment faults are becoming better constrained, much less is known about the tectonic and magmatic conditions that lead to fault abandonment. Here we present results from near-bottom investigations using the submersible *Alvin* and autonomous underwater vehicle (AUV) *Sentry* at a recently extinct detachment fault near 13°48'N, Mid-Atlantic Ridge, that allow documentation of the final stages of fault activity and magmatism. Seafloor imagery, sampling and near-bottom magnetic data show that the detachment footwall is intersected by an ~850 m wide volcanic outcrop including pillow lavas. Saturation pressures in these vesicular basalts, based on dissolved H_2O and CO_2, are less than their collection pressures, which could be explained by eruption at a shallower level than their present depth. Sub-bottom profiles reveal that sediment thickness, a loose proxy for seafloor age, is ~2 m greater on top of the volcanic terrain than on the footwall adjacent to the hanging-wall cutoff. This difference could be explained by current-driven erosion in the axial valley, or by continued slip after volcanic emplacement, either on a newly formed or pre-existing fault. Since current speeds near the footwall are unlikely to be sufficient to cause significant erosion, we favor the hypothesis that detachment slip continued after the episode of magmatism, consistent with growing evidence that oceanic detachments can continue to slip despite hosting magmatic intrusions.

1. Introduction

Exhumation of deep crustal rocks in the footwall of large-offset normal faults called detachments, leading to the formation of structures termed core complexes, was first recognized in the continents (Coney, 1974; Coney & Harms, 1984; Lister & Davis, 1989). Domed bathymetric highs on slow- and ultraslow-spreading mid-ocean ridges were later identified as oceanic core complexes (OCCs), with similar dimensions, fault geometry, and exhumation to those in terrestrial settings (e.g. Dick, 1989; Karson & Dick, 1983; Tucholke & Lin, 1994). Now recognized along large portions of Atlantic, Indian and Arctic Ocean spreading centers, oceanic detachment faults are commonly thought to exhume lower crustal and upper mantle rocks to the seafloor (Blackman et al., 1998; Cannat et al., 2006; Dick, 1989; Karson & Dick, 1983; Tucholke et al., 1998). Many domed OCCs have been documented at mid-ocean ridges (MORs)

and are often characterized by corrugations extending up to tens of kilometers parallel to the spreading direction, leading to the definition of a distinct mode of seafloor spreading (Escartín et al., 2008; Escartín & Canales, 2011; Ohara et al., 2001; Smith et al., 2006). OCC domes are spatially discrete features, consisting of a ridge-parallel breakaway zone formed when the fault initiated, and a low-angle slip surface that extends towards the MOR axis (Blackman et al., 2009). The point at which the footwall emerges from the seafloor, called the hanging-wall cutoff (or termination), marks the most recently exposed portion of fault scarp near the spreading axis. The total spreading-parallel extent of exposed fault surface suggests that detachments can accommodate plate spreading on timescales of 1–2 Ma, reflecting cycles of initiation, maintenance and cessation of slip (MacLeod et al., 2009; Okino et al., 2004; Tucholke et al., 1998). The final stages of this detachment fault cycle are poorly understood, with ongoing debate about whether slip ceases abruptly due to an increase in magmatism, or can continue following the intrusion of magmatic bodies such as dikes and sills (Bonnemains et al., 2017).

Numerical models predict that the style of crustal accretion is sensitive to the fraction of plate separation accommodated by dike intrusion, and initiation and maintenance of OCCs may be driven by variations in magma supply (Buck et al., 2005; Tian & Choi, 2016; Tucholke et al., 2008). Other models show that the rate of magma intrusion into the brittle lithosphere controls fault evolution, while dike injection into deeper layers only controls the lithology of exhumed material, meaning that OCC formation can be supported even when magma supply at deeper levels is high (Olive et al., 2010). Even where total magma supply is constant, focusing of melt by lateral dike propagation may influence the maintenance or cessation of slip on detachment faults (MacLeod et al., 2009), although this concept is yet to be quantitatively tested.

Here, we document the final tectonic and magmatic events associated with the detachment fault system at 13°48’N on the Mid-Atlantic Ridge (MAR), which has recently become inactive (Figure 1). Previous studies have identified numerous OCCs along this segment of the MAR, with seafloor mapping and seismicity patterns suggesting that nearby detachment faults at 13°20’N and 13°30’N are presently, or were very recently, active (Craig & Parnell-Turner, 2017; Escartín et al., 2003b; Parnell-Turner et al., 2017; Smith et al., 2003). We use detailed near-bottom bathymetric, magnetic, and CHIRP (Compressed High Intensity Radar Pulse) sub-bottom

data acquired by autonomous underwater vehicle (AUV) *Sentry* to map the exposed fault surface in detail. We analyze *in-situ* samples collected by deep submergence vehicle (DSV) *Alvin* and constrain the eruption pressure of basalts overlying the OCC using dissolved volatile concentrations (e.g., Dixon et al., 1988). These combined observations are used to assemble a coherent series of events surrounding the cessation of slip on this detachment fault.

1.1 Geological setting and prior observations

The corrugated dome of the 13°48'N OCC is located east of the MAR axial valley, and was first identified in shipboard multibeam bathymetric data (Figure 1; Smith et al., 2006, 2008). Low acoustic backscatter in towed sidescan sonar images acquired on top of the dome is consistent with a thick cover of sediment, interpreted to reflect fault inactivity (MacLeod et al., 2009; Mallows & Searle, 2012). Two north-south trending faults (f1 and f2, at 44.93°W and 44.95°W, respectively; Figure 1), which cut across the corrugated dome, have been previously identified based upon deep-towed sidescan sonar data (MacLeod et al., 2009; Mallows & Searle, 2012). Since corrugations continue westwards beyond both of these faults, the hanging-wall cutoff is thought to lie to the west, closer to the axis (Mallows & Searle, 2012). Rock samples, acquired *in-situ* using a seabed rock drill from the western part of the domed surface, are composed of hydrothermally altered peridotite, while basalt, diabase and trondjhemite were recovered from the eastern massif (MacLeod et al., 2009). These spatial observations and samples led Macleod et al. (2009) to conclude that tectonic spreading ceased at the 13°48′N OCC in the past 0.4–0.9 Ma, and has since been superseded by magmatic accretion at the ridge axis.

2. Methods

As part of a wider study of the occurrence of volatile-rich lavas on the MAR near 14°N during RV *Atlantis* cruise AT33-03, the OCC at 13°48'N was surveyed in detail by *Sentry* during dive 374 and sampled during *Alvin* dive 4822 in March 2016.

2.1 Near-bottom geophysical data

Sentry surveyed at 60–65 m above the seafloor at a speed of ~0.8–1.0 m/s, acquiring bathymetric data using a 400 kHz Reson 7125 multibeam sonar. These data were processed using MB-System software, and gridded at 1 m node spacing (Figure 2a; Caress & Chayes, 1996).

Magnetic data were acquired using a set of three, three-axis digital fluxgate magnetometers carried by *Sentry*. These data were gridded at 50 m, upward continued to a uniform depth plane (2500 m below sea level; Guspi, 1987), and inverted for crustal magnetization assuming a 100 m thick source layer following the approach of Tivey et al. (1993) (see Supplementary Material for full methods). The final magnetization solution was obtained by applying an annihilator, which accounts for ambiguity in the inversion, and yields a positive magnetization since the crust is assumed to be <781 ka old, i.e. formed after the Bruhnes-Matuyama reversal and thus is normally polarized (Figure 2c; Parker & Huestis, 1974).

Sidescan sonar data were acquired by *Sentry* using an Edgetech 2200M unit operating at dual frequencies of 120 and 410 kHz (Figure 3). CHIRP data were acquired simultaneously with sidescan data, as part of the Edgetech system, with a frequency sweep of 4–24 kHz, yielding a vertical resolution of ~10 cm; lithology-dependent penetration is expected to be < 10 m (Figure 4). CHIRP data were processed using MB-System and SeismicUnix software (Caress & Chayes, 1996; Cohen & Stockwell, 2013). Processing consisted of applying a zero-phase, sine-squared bandpass filter (frequencies 0.05, 0.1, 30, 35 kHz) to remove noise from other instruments on the vehicle; time-dependent linear gain; trace balance; clipping of extreme trace values; and depth conversion using a constant (water) velocity of 1500 m s^{-1}, following Parnell-Turner et al. (2014). The resulting SEG-Y format data were interpreted using OpendTect software.

2.2 Geological sampling and analysis

Ten *in-situ* rock samples (AL4822-060 to AL4822-069), one push core, and video and still photographic images were acquired during *Alvin* dive 4822 (track and sample locations are shown in Figure 2a). Major elements were analyzed at Boise State University using a Cameca SXFive electron microbe (Table 1). Dissolved CO_2 and H_2O concentrations within quenched rinds of the recovered glassy basalt samples were measured using the Cameca 1280 Secondary Ion Mass Spectrometer at the Northeast National Ion Microprobe Facility at Woods Hole Oceanographic Institution (WHOI), using methods based on Hauri et al. (2002) (see Supplementary Material for full methods and Table 1 for results). The presence or absence of vesicles was determined on 10× magnification reflected-light photomicrographs of polished glass fragments from the outer quenched 1 cm of the lava samples (Figure 5h). The exsolved

148 CO_2 content was measured at the Isotope Geochemistry Facility at WHOI for samples AL4822-
149 064 and AL4822-066 by capacitance manometry during in-vacuo crushing of the glass chips.

150 # 3. Results

151 ## 3.1 Near-bottom bathymetric data

152 Near-bottom bathymetric data show the detailed terrain of the 13°48'N OCC (Figure 2a), which
153 includes well-developed, curved, NW-SE trending hanging-wall cutoff that is clearly imaged
154 near the western edge of the *Sentry* survey, marking the separation between the footwall and
155 hanging wall of the detachment fault. East of the hanging-wall cutoff, the footwall rises upwards
156 with a slope of ~15°, and is cut by a series of linear channel-like features that may result from
157 local mass-wasting (Figure 2a). Slumping and sliding is also evident from numerous rubble
158 blocks and abundant talus on the seafloor recorded by *Alvin* dive video, and also the irregular
159 sidescan sonar returns, with patches of high backscatter probably indicating loose rubble and
160 scree (Figure 3a).
161
162 The scarp of fault f2 is located ~1 km east of the hanging-wall cutoff, and caused navigational
163 problems for *Sentry* (see data gaps at 44.953°W in Figure 2a). This scarp marks the western
164 edge of a series of smooth, roughly equant domes typically 150–200 m in diameter, which
165 coalesce to form a ~800 m-wide terrain with ~150 m relief, and a broad ring-shaped feature
166 centered on 44.95°W, 13.813°N (Figure 2a). This series of domes corresponds to the N-S
167 trending bathymetric high previously interpreted as a normal fault (MacLeod et al., 2009;
168 Mallows & Searle, 2012). The circular bathymetric geometry (Figure 2a), high crustal
169 magnetization (Figure 2c), and *in-situ* pillow basalts (Figure 5a) demonstrate that at least the
170 upper portion of this bathymetric high is volcanic in origin rather than tectonic as suggested by
171 MacLeod et al. (2009) and Mallows & Searle (2012). Scalloped bathymetry (example at
172 13.812°N; Figure 2a), and the presence of mass-wasted debris on the slope to the west, from
173 *Alvin* dive video and sidescan sonar backscatter imagery (Figure 3), support the interpretation
174 that fault f2 has partly displaced the volcanic domes, suggesting that slip on the fault took place
175 after volcanic emplacement. Bathymetric profiles over this terrain show that it has an overall
176 eastwards slope of ~10°, i.e., likely back-tilted relative to the footwall dip (Figure 2b). East of
177 this volcanic feature, the seafloor rises upwards with a slope of ~16°, and is remarkably smooth

in comparison to seafloor between the hanging-wall cutoff and the volcanic cones. We interpret this area to represent a continuation of the detachment fault footwall, which extends ~10 km eastwards towards the breakaway and is characterized by kilometer-scale corrugations (Figure 1).

3.2 Crustal magnetization

Near-bottom magnetic data acquired by *Sentry* provide insight into lithological variations across the 13°48'N OCC. High magnetization intensity is seen at the western edge of the *Sentry* survey, probably associated with a hanging wall composed of basaltic material (Figure 2c). Immediately east of the hanging-wall cutoff, magnetization is very low, consistent with a footwall composed of poorly magnetized crustal gabbro or mantle peridotite that has undergone low-temperature serpentinization (Klein et al., 2014; Szitkar & Dyment, 2014). A north-south oriented magnetization intensity high (~15 A m^{-1}) coincides with the series of domes at 44.95°W, flanked to the east by an area of low magnetization. This pattern of magnetization is consistent with a volcanic origin for the domes at the center of *Sentry* dive 374, with relatively poorly magnetized footwall material to the east and west.

3.3 Sediment cover

Sediment thickness is a rough proxy for seafloor exposure time, assuming that sediment is delivered at a constant rate to the seafloor from the water column, and is not significantly disturbed post-deposition by bottom currents. Assuming that sediments were uniformly deposited and undisturbed since emplacement, meter-scale variations in sediment thickness revealed in CHIRP data acquired by *Sentry* can be used to reconstruct the history of seafloor exposure by fault slip, volcanism or erosion. This method has been used to demonstrate active slip on a detachment fault at 16°36'N on the MAR, since sediment progressively thickens on the footwall from zero to ~2 m up-dip from the hanging-wall cutoff (Parnell-Turner et al., 2014).

CHIRP sub-bottom profiles reveal changes in the character and thickness of sediments overlying the detachment fault surface. Three discrete domains of sedimentary cover can be identified, consisting of the volcanic terrain, and the footwall to the east and west, which can be distinguished based upon their thickness and acoustic character (Figure 3). In the western part of the exposed footwall, adjacent to the hanging-wall cutoff, the seabed reflection has moderate

amplitude where sediment is present, and is diffuse and low in amplitude where sediment is absent (e.g. Figures 4b,c). This weak character is probably due to uneven seafloor leading to scattering of energy and hence a diffuse reflection, which may arise due to local mass-wasting and irregular sediment cover on this portion of the footwall. Sediment accumulations in this area are mostly acoustically transparent and lie above a basement that is marked by increased amplitude, but lacks any coherent internal reflectivity; they are thin or absent, ranging in thickness from 0 to 3.8 m, with a mean of 1.3 ± 0.5 m (uncertainty is 1σ calculated from spot measurements spaced ~1 m apart along profiles in Figure 3).

In contrast, volcanic terrain at the center of the survey is consistently blanketed by sediment 0.2–7.4 m thick, with a mean thickness of 3.3 ± 1.4 m (Figure 4i). The seafloor reflection on the volcanic terrain is bright in amplitude, and its attenuating character appears to cause the underling reflections to have weaker amplitude. Nonetheless, a clear transition in reflectivity can be identified beneath the seabed, which is interpreted to represent the basement reflection, which can be mapped over most of the volcanic terrain (Figures 4j,k).

East of the volcanic terrain, a third domain is evident where the seafloor reflection is very bright in amplitude, which in most places obscures any reflectivity below (Figure 4d). This strong reflection indicates a sediment-water interface with greater acoustic impedance contrast, which could be explained by an increased degree of cementation, and may explain its smooth appearance in the microbathymetry data. Where present, the basement reflection is relatively coherent, and indicates a sediment thickness that varies from 0.2–9 m (Figure 4e), with a mean thickness of 4.1 ± 1.9 m.

3.4 Lithology and geochemistry

The western part of the *Sentry* survey area is dominated by basalt boulders in a sedimented talus field below the main scarp of fault f2 (Figure 2a), based on the *Alvin* rock sampling. Samples AL4822-060 to AL4822-063 from this area are sparsely phyric basalts with rare rounded vesicles, and devoid of glass. Samples AL4822-064 to AL4822-067 were collected on the volcanic terrain, composed of stacked pillows (and tentatively dikes), where individual basalt tubes and pillows protrude through the sediment cover above the scarp (Figure 5a). The suite of

basalt samples is relatively fresh, with glass showing only moderate surface palagonite, and most samples have a thin Mn-oxide coating. Samples AL4822-064 to AL4822-067 exhibit a narrow range in glass major element and volatile compositions (e.g. SiO_2 = 52.90–53.58 wt.%; MgO = 8.19–8.28 wt.%; H_2O = 0.088–0.092 wt.%; CO_2 = 102–106 ppm; Table 1). Vesicles are present in the outer quenched margin of each basalt sample collected from the volcanic terrain (example shown in Figure 5g) and the CO_2 released by crushing ranged from 48–183 ppm. The saturation pressure derived from the dissolved CO_2 and H_2O concentrations is ~5 MPa less than the collection pressure (equivalent to a depth of ~500 m with seawater density 1.027 g/cm^3), based on VolatileCalc and *SolEx* models (Dixon et al., 1995; Newman & Lowenstern, 2002; Witham et al., 2012). These solubility models are applicable for basalts with <52 wt.% SiO_2, which is slightly exceeded in these samples. The solubility models presented by Ghiorso & Gualda (2015) and Papale et al. (2006) yield greater differences between the saturation pressure and collection pressure (>10 MPa). Although there are uncertainties associated with these solubility models due to the compositional extrapolation, these lavas are likely to be undersaturated in volatiles at their collection depth to some degree.

Samples AL4822-068 and AL4822-069 were collected up-dip of the volcanic terrain on the eastern footwall, from a hummocky outcrop of hydrothermally altered peridotite and trondhjemite, situated on a sedimented slope (Figure 5b-f). In these samples, peridotite is completely altered to serpentine and magnetite with minor chlorite, while talc-alteration is most pronounced on rock surfaces forming centimeter-sized coronas. In addition, talc penetrates the interior along monomineralic veins and occurs together with serpentine in bastite texture after orthopyroxene (Figures 5c,d). Shear phacoids, non-pseudomorphic textures and kinked veins indicate that tectonic movements postdate serpentinization and talc-alteration. Trondhjemite from this outcrop consists of albitic plagioclase, quartz, chlorite, and anatase (Figures 5e,f). Plagioclase and quartz contain abundant fluid inclusions and amphibole, which is possibly altered to quartz and chlorite. Millimeter-sized crack-seal veins cutting across the trondhjemite are composed of coarse grained, inclusion free quartz, that also reach adjacent serpentinite.

The single push core sample collected during *Alvin* dive 4822 (AL4822-PC07) was collected on the north-facing slope of the volcanic terrain near sample site AL4822-063 (Figure 2a).

Penetrating 19 cm, this core consists of very fine-grained mud devoid of any visible layering or grading, is black to tan in color, with a covering of black and white shells in the top ~ 5 cm. The location and shallow penetration of this core mean that it does not provide sufficient calibration for the CHIRP sediment images.

4. Discussion

4.1 Volcanism on detachment footwall

Imaging and sampling of *in-situ* pillow basalts, and observed high magnetization in near-bottom *Sentry* data indicate that bathymetric domes at the center of the survey area are volcanic in origin, apparently cross-cutting the detachment surface. The surficial volcanism does not preclude the presence of an underlying north-south trending normal fault as suggested by MacLeod et al. (2009), and may be responsible for the large scarp, f2. This fault may have begun as a magma-filled crack that propagated through the detachment footwall, and later fault activity may have offset volcanic outcrops leading to recent mass-wasting. West of this volcanic terrain, corrugated bathymetry and shallow slopes suggest that an additional section of inactive detachment fault is exposed, bounded to the west by a well-defined hanging-wall cutoff (Figure 2).

Most MORB display saturation pressures roughly equal to their collection pressures due to equilibrium degassing, or saturation pressures greater than their collection pressures due to short timescales for magma ascent and emplacement relative to timescales for CO_2 diffusion into bubbles (Dixon et al., 1988). Some MORB samples display saturation pressures less than their collection pressures and do not contain exsolved volatiles, probably because the magma never reached volatile saturation (e.g. Michael & Graham, 2015). Lavas collected from the 13°48'N OCC are unusual given that saturation pressures are less than the collection pressures despite the presence of exsolved volatiles (Figure 6). Based on VolatileCalc and *SolEx* results, these saturation pressures are not highly sensitive to temperature, initial volatile concentrations, or degassing path (i.e., open vs. closed system) (Dixon et al., 1995, Newman and Lowenstern, 2002, Witham et al., 2012). Interpretation of calculated saturation pressures relative to collection pressures assumes that solubility model uncertainties are <10%, and that the high silica content (~53 wt. %) relative to the model calibration (i.e., up to 49 wt. %) does not affect H_2O and CO_2

298 solubility. Several hypotheses could explain the shallow saturation pressures relative to
299 collection pressures (Figure 7) and the change in sediment thickness on either side of the
300 volcanic terrain (Figure 3). Lavas could have been erupted at a shallower depth, equilibrated
301 with that pressure and then flowed downslope; or the magma feeding the lava flows could have
302 reached (and equilibrated at) a shallower depth during dike intrusion, but erupted at their current
303 position. Both of these hypotheses are implausible, however, given that the exsolved gas likely
304 would have equilibrated with the melt at the present depth. Based on the volatile concentrations
305 alone, the most likely scenario is that the lavas were emplaced ~500 m shallower than their
306 present depth and subsequently downthrown on an up-dip fault. The only candidate fault near
307 this scale is f1, which only has up to 200 m of vertical displacement, but can be traced in towed
308 sidescan data upslope of the volcanic deposit (Figure 1, and MacLeod et al., 2009).
309
310
311 **4.2 Timing of volcanism and fault deactivation**
312 Thin (1.3 ± 0.5 m) sediments over the western part of the detachment fault surface may indicate
313 that little time has passed since its exposure for sediment to accumulate, consistent with earlier
314 sidescan sonar observations (MacLeod et al., 2009). Since sediment covering the volcanic terrain
315 to the east is thicker (3.3 ± 1.4 m) than that covering the western footwall, slip on the detachment
316 fault may have continued after emplacement of the volcanic outcrop. In this interpretation, the
317 ~2.5 km span of seafloor between the western edge of the volcanic terrain and the hanging-wall
318 cutoff must have been exhumed in the period between volcanic emplacement and cessation of
319 detachment slip (Figures 7b,c). Assuming 30% spreading asymmetry and a full spreading rate of
320 25.5 km Ma^{-1} (Mallows and Searle, 2012), we estimate that the fault continued to slip for ~150
321 ka after magmatic emplacement.
322
323 Piston cores located between 10° and 15°N indicate that the sediment accumulation rate since
324 Marine Isotope Stage 5 (130 ka) is 7 ± 2 mm ka^{-1} (Damuth, 1977). Hence the 1.3 ± 0.5 m of
325 sediment cover imaged on the western edge of the detachment footwall suggests that this fault
326 surface has been inactive for 185 ± 89 ka. However, the potential effects of mass wasting in the
327 area make this estimate uncertain. Summing the final period of slip (~150 ka, see above) and
328 period of fault inactivity gives an age of emplacement for the volcanic terrain of 335 ± 89 ka,

329 which is broadly consistent with the observed 3.3 ± 1.4 m of sediment cover there, which would
330 accumulate over an interval of 470 ± 123 ka. These age estimates are under-constrained due to
331 the lack of a more accurate local sedimentation rate estimate, however, the observed relative
332 differences in sediment thickness are robust if sedimentation rate has been constant over the past
333 ~500 ka. The contrasting sediment cover across the volcanic terrain and western footwall
334 provides evidence for detachment fault slip after emplacement of the volcanic terrain. This
335 hypothesis, however, is not consistent with the undersaturated volatile content of basalts from the
336 volcanic edifice.
337
338 A key assumption in the sediment accumulation proxy is that sediments observed over the
339 western footwall retain their original, uniform depositional thickness, and have not been
340 significantly modified by mass-wasting or erosion. *Alvin* dive video and sidescan sonar data
341 indicate that sediments on the western footwall are covered in patchy rubble and talus (Figure 3),
342 suggesting that basement material may have undergone mass wasting, in particular near steep
343 scarps such as at fault f2 (Figure 2). These scarps and talus fields may have led to variations in
344 initial sediment thickness, as fine-grained material may have ponded within local bathymetric
345 hollows or adjacent to steep scarps (for example of apparent ponding see Figure 4c).
346
347 We cannot rule out the possibility that sediment on the western footwall was originally of similar
348 thickness to that on the volcanic terrain, and has subsequently been eroded by mass-wasting or
349 redistributed by bottom currents. If the sediment on the western footwall and volcanic terrain
350 were originally of equal thickness, then volcanic emplacement must have been contemporaneous
351 with the cessation of detachment fault slip, and activity at the 13°48'N OCC must have ended at
352 a similar time to the volcanism at 470 ± 123 ka. In this case, volcanic material probably
353 breached the corrugated detachment surface at this time, and erupted ~2.5 km east of the
354 hanging-wall cutoff (Figure 7d). Post eruption, the volcanic edifice was downthrown by ~500 m
355 by a fault, f1 (Figure 1), consistent with the observed lava volatile content (Figure 7e). Thin or
356 absent sediments on the footwall west of the volcanic edifice are therefore explained by post-
357 depositional mass wasting and transport, possibly by strong bottom currents within the axial
358 valley (Figure 7e). In this interpretation, the back-tilt of the volcanic terrain (Figure 2b) would

result from clockwise tilt as the volcanic material was down-thrown towards the axis as a contiguous block after emplacement.

Deep-water flow speed measurements, experimental data and theoretical arguments show that the onset of surface erosion of mud and silt is likely to occur at current velocities above 10–12 cm s^{-1}, while velocities of > 30 cm s^{-1} are required to remove all but the sand fraction (Gross & Williams, 1991; McCave & Hall, 2006). Axis-parallel flow speeds measured in a similar settings on the Mid-Atlantic Ridge are much lower than these erosional thresholds, averaging 2 cm s^{-1} near 29°N (Murton et al., 1999), and 5–6 cm s^{-1} near the Rainbow hydrothermal vent field (German et al., 1998). Since direct observations of flow speed are not available near 13°48'N, vehicle dynamics from *Sentry* provide a qualitative way to estimate modern current strength during the dive. Supplementary Figure 19 shows that the *Sentry*'s heading closely matched trackline heading throughout dive 374, both during east-west and north-south directions of travel. This observation suggests that there were no strong east-west or north-south flowing currents acting during the dive, although this finding does not rule out stronger currents in the past. Hence on balance, we suggest that erosion of sediment may have been negligible in the region of the 13°48'N OCC footwall.

5.3 Mechanism for Halting Detachment Fault Slip

Seafloor observations at the nearby 13°30'N OCC show that the end of slip was probably caused by lateral propagation of neovolcanic ridges and dikes along strike within the axial valley, which cut across the emerging corrugated surfaces (MacLeod et al., 2009). At the toe of the 13°30'N OCC, chilled diabase dikes have also been mapped and sampled in the hanging wall above the detachment footwall, and are interpreted to represent syn- or post-uplift magmatic intrusion (Bonnemains et al., 2017). A series of normal faults oriented perpendicular to corrugations have cut across the dome near to the hanging-wall cutoff, three of which have propagated across the OCC tip to define a small local graben (Escartín et al., 2017). Elsewhere, at IODP Hole 1309B on Atlantis Massif (also on the MAR), a series of sill-like bodies and diabase dikes were encountered, which are thought to have been emplaced during late stages of slip there (Blackman et al., 2011; Ildefonse et al., 2007). Steeply dipping lithological contacts in Hole 1309D provide

388 further evidence that late basaltic intrusions were intruded sub-parallel to the steep portion of the
389 fault (McCaig et al., 2010).
390
391 Evidence for a punctuated sequence of slip, volcanism and renewed slip can be found at other
392 extinct detachments, for example at Mount Dent on the Mid-Cayman Spreading Center (MCSC).
393 A low seismic velocity anomaly 5 km beneath the Mount Dent massif and Von Dam Vent Field
394 can be explained either by reduced magmatism leading to a cracking front and deep fluid
395 circulation, or by intrusive magmatic sills (Harding et al., 2017). Although either hypothesis
396 would lead to a cessation of slip and is equally valid, the link between changing magma supply
397 and fault slip is comparable with observations at 13°48'N. At the nearby Mount Hudson OCC
398 (also on the MCSC), the youngest portion of the detachment fault surface is cross-cut by an axial
399 volcanic ridge, marked by a line of conical volcanic edifices (Cheadle et al., 2012; Hayman et
400 al., 2011). The relative positions of the hanging-wall cutoff and volcanic terrains at Hudson
401 Dome, and the 13°48'N OCC described here, are strikingly similar, suggesting a sequence of
402 volcanic emplacement, short-lived fault slip and final halting. Hence in the later stages of OCC
403 formation, increased magmatism may episodically bring lavas to the surface, perhaps following
404 cracks and faults within the footwall. At 13°48'N and at Hudson Dome, this eruptive phase may
405 have been followed by a brief period of detachment slip (on 100 ka timescale), prior to the final
406 halting of slip altogether (Cheadle et al., 2012). This final phase of fault slip may come to an end
407 once magma supply increased so that extension is preferentially taken up by expansion of
408 magma-filled dikes within the axial valley. Finally, evidence of contemporaneous magmatism
409 and fault slip is found at the 15°45'N OCC on the MAR, where undeformed diabase dikes with
410 chilled margins cross-cut the corrugated detachment surface (Escartín et al., 2003a). These dike
411 intrusions are thought to have been restricted spatially and temporally, so that the detachment
412 footwall may have continued to slip as a single cohesive unit, thus retaining mechanical integrity.
413

414 ## 6. Conclusions

415
416 We have used near-bottom geophysical and lithological observations acquired by AUV and
417 submersible dives at a domed core complex on the MAR to reconstruct the final stages of

418 volcanism and faulting on an inactive OCC. Photographs and sampling of *in-situ* basalt pillows,
419 and high magnetization recorded in near-bottom AUV data confirm that the 13°48'N OCC is
420 cross-cut by an ~850 m-wide volcanic terrain, which also coincides with an axis-parallel normal
421 fault. Bathymetric corrugations are observed east and west of this feature, while ultramafic
422 lithologies have been sampled and drilled nearby, confirming the presence of an exhumed
423 detachment footwall.
424
425 CHIRP sub-bottom profile images show that sediment thickness varies across the detachment
426 fault system, which is used here as a rough proxy for seafloor exposure time. The saturation
427 pressures from dissolved H_2O and CO_2 in vesicular lavas sampled on the footwall are less than
428 the collection pressures, which could be explained by a depth increase since emplacement due to
429 secondary faulting (Figures 7d,e). If sediments on the western footwall are undisturbed by mass-
430 wasting and redistribution by bottom currents, then the differences in sediment thickness imply
431 that this section of the fault must have been exhumed after volcanic emplacement, implying that
432 detachment fault activity continued for ~150 ka after volcanism. We favor this hypothesis since
433 there is no evidence for the high flow speeds required to remove sediment from the western
434 footwall, and it is consistent with evidence of slip after magmatism at OCCs elsewhere.
435 Although the episode of magmatism must have been insufficient to immediately halt slip on the
436 detachment fault, the association between changing magma supply and fault inactivity may apply
437 to OCCs in general.
438

439 ## Acknowledgements

440 Data will be available online from the Marine Geoscience Data System (MGDS). We gratefully
441 acknowledge the dedicated personnel associated with R/V *Atlantis*, AUV *Sentry*, and DSV *Alvin*,
442 and the entire scientific party of the Popping Rocks cruise, AT33-03. We thank N. Hayman and
443 an anonymous reviewer for their helpful comments. Seagoing and analytical efforts were
444 supported by National Science Foundation grants OCE-1259218, OCE-1260578 and OCE-
445 1736547.

References

Blackman, D. K., Canales, J. P., & Harding, A. J. (2009). Geophysical signatures of oceanic core complexes. *Geophys. J. Int.*, *178*(2), 593–613. https://doi.org/10.1111/j.1365-246X.2009.04184.x

Blackman, D. K., Cann, J. R., Janssen, B., & Smith, D. K. (1998). Origin of extensional core complexes: Evidence from the Mid-Atlantic Ridge at Atlantis Fracture Zone. *J. Geophys. Res.*, *103*(B9), 21,315-321,333.

Blackman, D. K., Ildefonse, B., John, B. E., Ohara, Y., Miller, D. J., Abe, N., … Zhao, X. (2011). Drilling constraints on lithospheric accretion and evolution at Atlantis Massif, Mid-Atlantic Ridge 30°N. *J. Geophys. Res.*, *116*(B07103). https://doi.org/10.1029/2010JB007931

Bonnemains, D., Escartín, J., Mével, C., Andreani, M., & Verlaguet, A. (2017). Pervasive silicification and hangingwall overplating along the 13°20' N oceanic detachment fault (Mid-Atlantic Ridge). *Geochem. Geophys. Geosyst*, *18*, 2028–2053. https://doi.org/10.1002/2017GC006846

Buck, W. R., Lavier, L., & Poliakov, A. N. B. (2005). Modes of faulting at mid-ocean ridges. *Nature*, *434*, 719–723. https://doi.org/10.1038/nature03358

Cannat, M., Sauter, D., Mendel, V., Ruellan, E., Okino, K., Escartín, J., … Balaa, M. (2006). Modes of seafloor generation at a melt-poor ultraslow-spreading ridge. *Geology*, *34*, 605–608. https://doi.org/10.1130/G22486.1

Caress, D. W., & Chayes, D. L. (1996). Improved Processing of Hydrosweep DS Multibeam Data on the R/V Maurice Ewing. *Mar. Geophys. Res.*, *18*, 631–650.

Cheadle, M. J., John, B. E., German, C. R., & Kusznir, N. J. (2012). The Death Throes of Ocean Core Complexes: Examples from the Mid-Cayman Spreading Centre. *Abstract OS11E-01 Presented at 2012 Fall Meeting, AGU, San Francisco, Calif. 5-9 Dec*.

Cohen, J. K., & Stockwell, J. W. (2013). *CWP/SU: Seismic Un*x. Release No. 43R5: an open source software package for seismic research and processing*. Center for Wave Phenomena, Colorado School of Mines.

Coney, P. J. (1974). Structural analysis of the Snake Range "décollement," east-central nevada. *Bull. Geol. Soc. Am.*, *85*(6), 973–978. https://doi.org/10.1130/0016-7606(1974)85<973:SAOTSR>2.0.CO;2

Coney, P. J., & Harms, T. A. (1984). Cordilleran metamorphic core complexes: Cenozoic extensional relics of Mesozoic compression. *Geology*, *12*(9), 550–554. https://doi.org/10.1130/0091-7613(1984)12<550:CMCCCE>2.0.CO;2

Craig, T. J., & Parnell-Turner, R. (2017). Depth-varying seismogenesis on an oceanic

481 detachment fault at 13°20'N on the Mid-Atlantic Ridge. *Earth Planet. Sci. Lett.*, *479*, 60–
482 70. https://doi.org/10.1016/j.epsl.2015.01.026

483 Damuth, J. E. (1977). Late Quaternary sedimentation in the western equatorial Atlantic Late
484 Quaternary sedimentation in the western equatorial Atlantic. *Geol. Soc. Am. Bull.*, *88*, 695–
485 710.

486 Dick, H. J. B. (1989). Abyssal peridotites, very slow spreading ridges and ocean ridge
487 magmatism. *Geol. Soc. Spec. Pub.*, *42*, 71–105.
488 https://doi.org/10.1144/GSL.SP.1989.042.01.06

489 Dixon, J. E., Stolper, E. M., & Delaney, J. R. (1988). Infrared spectroscopic measurements of
490 CO_2 and H_2O in Juan de Fuca Ridge basaltic glasses. *Earth Planet. Sci. Lett.*, *90*, 87–104.
491 https://doi.org/10.1016/0012-821X(88)90114-8

492 Dixon, J. E., Stolper, E. M., & Holloway, J. R. (1995). An Experimental Study of Water and
493 Carbon Dioxide Solubilities in Mid-Ocean Ridge Basaltic Liquids. Part II: Applications to
494 Degassing. *J. Petrol.*, *36*, 1607–1631.
495 https://doi.org/10.1093/oxfordjournals.petrology.a037268

496 Escartín, J., & Canales, J. P. (2011). Detachments in oceanic lithosphere: Deformation,
497 magmatism, fluid flow, and ecosystems. *Eos Trans., AGU*, *92*(4), 31.

498 Escartín, J., Mével, C., MacLeod, C. J., & McCaig, A. M. (2003a). Constraints on deformation
499 conditions and the origin of oceanic detachments: The Mid-Atlantic Ridge core complex at
500 15°45′N. *Geochem. Geophys. Geosyst*, *4*(8). https://doi.org/10.1029/2002GC000472

501 Escartín, J., Smith, D. K., Cann, J. R., Schouten, H., Langmuir, C. H., & Escrig, S. (2008).
502 Central role of detachment faults in accretion of slow-spreading oceanic lithosphere.
503 *Nature*, *455*(7214), 790–794. https://doi.org/10.1038/nature07333

504 Escartín, J., Smith, D. K., & Cannat, M. (2003b). Parallel bands of seismicity at the Mid-Atlantic
505 Ridge, 12–14°N. *Geophys. Res. Lett.*, *30*(12), 1620. https://doi.org/10.1029/2003GL017226

506 German, C. R., Richards, K. J., Rudnicki, M. D., Lam, M. M., & Charlou, J.-L. (1998).
507 Topographic control of a dispersing hydrothermal plume. *Earth Planet. Sci. Lett.*, *156*(3–4),
508 267–273. https://doi.org/10.1016/S0012-821X(98)00020-X

509 Gross, T. F., & Williams, A. J. (1991). Characterization of deep-sea storms. *Marine Geology*,
510 *99*(3–4), 281–301. https://doi.org/10.1016/0025-3227(91)90045-6

511 Guspi, F. (1987). Frequency-Domain Reduction of Potential Field Measurements to a Horizontal
512 Plane. *Geoexploration*, *24*, 87–98.

513 Harding, J. L., Van Avendonk, H. J. A., Hayman, N., Grevemeyer, I., Peirce, C., & Dannowski,
514 A. (2017). Magmatic-tectonic conditions for hydrothermal venting on an ultraslow-spread
515 oceanic core complex. *Geology*, *45*(9), 839–842. https://doi.org/10.1130/G39045.1

Hauri, E., Wang, J., Dixon, J. E., King, P. L., Mandeville, C., & Newman, S. (2002). SIMS analysis of volatiles in silicate glasses. *Chem. Geol.*, *183*, 99–114. https://doi.org/10.1016/S0009-2541(01)00375-8

Hayman, N., Grindlay, N., Perfit, M., Mann, P., Leroy, S., & De Lépinay, B. (2011). Oceanic core complex development at the ultraslow spreading Mid-Cayman Spreading Center. *Geochem. Geophys. Geosyst*, *12*(3). https://doi.org/10.1029/2010GC003240

Ildefonse, B., Blackman, D. K., John, B. E., Ohara, Y., Miller, D. J., & MacLeod, C. J. (2007). Oceanic core complexes and crustal accretion at slow-spreading ridges. *Geology*, *35*(7), 623–626. https://doi.org/10.1130/G23531A.1

Jones, M. R., Soule, S. A., Gonnermann, H. M., Le Roux, V., & Clague, D. A. (2018). Magma ascent and lava flow emplacement rates during the 2011 Axial Seamount eruption based on CO_2 degassing. *Earth Planet. Sci. Lett.*, *494*, 32–41. https://doi.org/10.1016/j.epsl.2018.04.044

Karson, J. A., & Dick, H. J. B. (1983). Tectonics of ridge-transform intersections at the Kane fracture zone. *Mar. Geophys. Res.*, *6*(1), 51–98. https://doi.org/10.1007/BF00300398

Klein, F., Bach, W., Humphris, S. E., Kahl, W. A., Jöns, N., Moskowitz, B., & Berquó, T. S. (2014). Magnetite in seafloor serpentinite-Some like it hot. *Geology*, *42*(2), 135–138. https://doi.org/10.1130/G35068.1

Lister, G. S., & Davis, G. A. (1989). The origin of metamorphic core complexes and detachment faults formed during Tertiary continental extension in the northern Colorado River region, USA. *J. Struct. Geol.*, *11*(112), 65–94.

MacLeod, C. J., Searle, R. C., Murton, B. J., Casey, J. F., Mallows, C., Unsworth, S. C., … Harris, M. (2009). Life cycle of oceanic core complexes. *Earth Planet. Sci. Lett.*, *287*(3–4), 333–344. https://doi.org/10.1016/j.epsl.2009.08.016

Mallows, C., & Searle, R. C. (2012). A geophysical study of oceanic core complexes and surrounding terrain, Mid-Atlantic Ridge 13°N-14°N. *Geochem. Geophys. Geosyst*, *13*. https://doi.org/10.1130/G39232.1

McCaig, A. M., Delacour, A., Fallick, A. E., Castelain, T., & Fruh-Green, G. L. (2010). Detachment Fault Control on Hydrothermal Circulation Systems: Interpreting the Subsurface Beneath the TAG Hydrothermal Field Using the Isotopic and Geological Evolution of Oceanic Core Complexes in the Atlantic. In P. A. Rona, C. W. Devey, & B. J. Murton (Eds.), *Diversity of Hydrothermal Systems on Slow Spreading Ocean Ridges* (pp. 207–239). Washington, D. C.: American Geophysical Union. https://doi.org/10.1029/2008GM000729

McCave, I. N., & Hall, I. R. (2006). Size sorting in marine muds: Processes, pitfalls, and prospects for paleoflow-speed proxies. *Geochem. Geophys. Geosyst*, *7*(10), 1984–1986. https://doi.org/10.1029/2006GC001284

553 Michael, P. J., & Graham, D. W. (2015). The behavior and concentration of CO2 in the
554 suboceanic mantle: Inferences from undegassed ocean ridge and ocean island basalts.
555 *Lithos*, *236–237*, 338–351. https://doi.org/10.1016/j.lithos.2015.08.020

556 Murton, B. J., Redbourn, L. J., German, C. R., & Baker, E. T. (1999). Sources and fluxes of
557 hydrothermal heat, chemicals and biology within a segment of the Mid-Atlantic Ridge.
558 *Earth Planet. Sci. Lett.*, *171*(2), 301–317. https://doi.org/10.1016/S0012-821X(99)00157-0

559 Newman, S., & Lowenstern, J. B. (2002). VolatileCalc: a silicate melt – H_2O – CO_2 solution
560 model written in Visual Basic for excel. *Computers & Geosciences*, *28*, 597–604.
561 https://doi.org/doi:10.1016/S0098-3004(01)00081-4

562 Ohara, Y., Yoshida, T., & Kasuga, S. (2001). Giant megamullion in the Perece Vela Backarc
563 basin. *Mar. Geophys. Res.*, *22*, 47–61.

564 Okino, K., Matsuda, K., Christie, D. M., Nogi, Y., & Koizumi, K. (2004). Development of
565 oceanic detachment and asymmetric spreading at the Australian-Antarctic Discordance.
566 *Geochem. Geophys. Geosyst*, *5*(12), doi:10.1029/2004GC000793.
567 https://doi.org/10.1029/2004GC000793

568 Olive, J. A., Behn, M. D., & Tucholke, B. E. (2010). The structure of oceanic core complexes
569 controlled by the depth distribution of magma emplacement. *Nature Geosci.*, *3*(7), 491–495.
570 https://doi.org/10.1038/ngeo888

571 Parker, R. L., & Huestis, S. (1974). The Inversion of Magnetic Anomalies in the Presence of
572 Topography. *J. Geophys. Res.*, *79*(11), 1587–1593.

573 Parnell-Turner, R., Cann, J. R., Smith, D. K., Schouten, H., Yoerger, D., Palmiotto, C., … Bai,
574 H. (2014). Sedimentation rates test models of oceanic detachment faulting. *Geophys. Res.*
575 *Lett.*, *41*. https://doi.org/10.1002/2014GL061555

576 Parnell-Turner, R., Sohn, R. A., Peirce, C., Reston, T. J., Macleod, C. J., Searle, R. C., & Simão,
577 N. (2017). Oceanic Detachment Faults Generate Compression in Extension. *Geology*, *45*,
578 932–926. https://doi.org/10.1130/G39232.1

579 Smith, D. K., Cann, J. R., & Escartín, J. (2006). Widespread active detachment faulting and core
580 complex formation near 13°N on the Mid-Atlantic. *Nature*, *442*, 440–443.
581 https://doi.org/10.1038/nature04950

582 Smith, D. K., Escartín, J., Cannat, M., Tolstoy, M., Fox, C. G., Bohnenstiehl, D. R., & Bazin, S.
583 (2003). Spatial and temporal distribution of seismicity along the northern Mid-Atlantic
584 Ridge (15°–35°N). *J. Geophys. Res.*, *108*(B3), doi:10.1029/2002JB001964.
585 https://doi.org/10.1029/2002JB001964

586 Smith, D. K., Escartín, J., Schouten, H., & Cann, J. R. (2008). Fault rotation and core complex
587 formation: Significant processes in seafloor formation at slow-spreading mid-ocean ridges
588 (Mid-Atlantic Ridge, 13°–15°N). *Geochem. Geophys. Geosyst*, *9*(3).
589 https://doi.org/10.1029/2007GC001699

590 Szitkar, F., & Dyment, J. (2014). Near-seafloor magnetics reveal tectonic rotation and deep
591 structure at the TAG (Trans-Atlantic Geotraverse) hydrothermal site (Mid-Atlantic Ridge,
592 26 N). *Geology*, *43*, 87–90. https://doi.org/10.1130/G36086.1

593 Tian, X., & Choi, E. (2016). Effects of axially variable diking rates on faulting at slow spreading
594 mid-ocean ridges. *Earth Planet. Sci. Lett.*, *458*, 14–21.
595 https://doi.org/10.1016/j.epsl.2016.10.033

596 Tivey, M. A., Rona, P. A., & Schouten, H. (1993). Reduced crustal magnetization beneath the
597 active sulfide mound, TAG hydrothermal field. *Earth Planet. Sci. Lett.*, *115*, 101–115.
598 Retrieved from http://www.sciencedirect.com/science/article/pii/0012821X9390216V

599 Tucholke, B. E., Behn, M. D., Buck, W. R., & Lin, J. (2008). Role of melt supply in oceanic
600 detachment faulting and formation of megamullions. *Geology*, *36*(6), 455.
601 https://doi.org/10.1130/G24639A.1

602 Tucholke, B. E., & Lin, J. (1994). A geological model for the structure of ridge segments in slow
603 spreading ocean crust. *J. Geophys. Res.*, *99*, 11,937-11,958.

604 Tucholke, B. E., Lin, J., & Kleinrock, M. C. C. (1998). Megamullions and mullion structure
605 defining oceanic metamorphic core complexes on the Mid-Atlantic Ridge. *J. Geophys. Res.*,
606 *103*(B5), 9857–9866.

607 Witham, F., Blundy, J., Kohn, S. C., Lesne, P., Dixon, J., Churakov, S. V., & Botcharnikov, R.
608 (2012). SolEx: A model for mixed COHSCl-volatile solubilities and exsolved gas
609 compositions in basalt. *Computers and Geosciences*, *45*, 87–97.
610 https://doi.org/10.1016/j.cageo.2011.09.021

611
612
613
614
615
616
617
618
619
620
621
622
623

624 **Figure Captions**

625

626 **Figure 1.** Bathymetry of Mid-Atlantic Ridge near 13°48'N oceanic core complex (Smith et al.,
627 2006). Inset: location of study site (black box) and plate boundaries (black lines). Main panel:
628 dashed line marks neovolcanic zone, interpretation from Mallows & Searle (2012) based on
629 deep-tow sidescan sonar data; black box is *Sentry* dive 374; star is location of volatile-rich
630 ('popping') rocks recovered during Cruise AT33-03; colored circles are samples acquired by
631 seabed rock drill (MacLeod et al., 2009); large black arrows show plate spreading direction;
632 small black arrows mark spreading-parallel corrugations; numbered white arrows show N-S
633 trending faults crossing corrugated dome.

634

635

636

637

638 **Figure 2**. Near-bottom bathymetry and magnetization at 13°48'N OCC acquired by AUV
639 *Sentry*. a) Bathymetry, gridded at 1 m x 1 m cell size, illuminated from northwest. Gray
640 line/colored dots are trackline/sampling sites from *Alvin* dive 4822, site numbers labeled without
641 AL4822- prefix; dashed lines show location of profiles in (b); black arrow marks hanging-wall
642 cutoff (hwc); white arrow marks fault scarp f2. b) Bathymetric profiles. c) Magnetization
643 intensity.

644

645

646

647

648 **Figure 3.** Sidescan sonar backscatter (gray shades) overlain with sediment thickness calculated
649 from CHIRP profiles acquired during *Sentry* dive 374. Colored dots indicate spot sediment
650 thickness estimates, spaced at ~1 m intervals along profiles; black dots indicate sediment of
651 unknown thickness; labeled black lines are track lines, numbered boxes show location of zooms
652 in Figure 4. Note the three distinct domains of sediment thickness, thickening from west to east.

653

654

655 **Figure 4.** CHIRP profiles from *Sentry* dive 374, locations of profiles and zooms shown in
656 Figure 3. Note vertical axis plotted relative to vehicle, as two-way travel time (TWTT) and depth
657 (assuming a velocity of 1500 m s^{-1}). (a) Line 0. Green lines are seabed with sedimentary
658 material beneath; red lines are sediment-basement interface where visible; boxes are zooms
659 shown below. (b) Thin sediment on west footwall; (c) apparent sediment pond on edge of
660 volcanic terrain; (d) highly reflective seabed with acoustically transparent subsurface on east
661 footwall; (e) highly reflective seabed with weak basement reflection indicating ~3 m thick
662 sediment on east footwall. (f) Line 4. (g) and (h) Clearly imaged ~1 m thick sediment on west
663 footwall. (i) Line 10. (j) and (k) Weak basement reflections beneath highly reflective seabed
664 show ~5 m thick sediment on volcanic terrain.
665
666
667
668 **Figure 5**. Outcrop photographs and rock samples from *Alvin* dive 4822. a) Pillow basalt outcrop
669 at site 67, located at top of volcanic terrain. b) Serpentinized peridotite outcrop at site 68, located
670 on eastern detachment footwall. c) Serpentinized peridotite hand specimen, site 68. Sample
671 underwent additional Si-metasomatism and weathering, leading to formation of talc, quartz,
672 hematite, and goethite. d) Thin section photomicrograph mosaic in cross-polarized transmitted
673 light of serpentinized peridotite, site 68. e) Hydrothermally-altered trondhjemite hand specimen,
674 site 69, located on eastern detachment footwall. f) Thin section photomicrograph mosaic in
675 cross-polarized transmitted light of hydrothermally altered trondhjemite from site 69, consisting
676 of albitic plagioclase, quartz, chlorite, and anatase. g) Reflected light photomicrograph of the
677 outer quenched margin of basalt sample 65. Dark gray is epoxy mount, light gray is basalt glass,
678 and black circles are vesicles within glass. h) Thin section photomicrograph in plane-polarized
679 transmitted light of glassy basalt from site 64.
680
681
682
683
684

685 **Figure 6.** Saturation pressure vs. sample collection pressure for pillow basalts collected from
686 13°48'N detachment footwall (red circles), compared to ultradepleted MORB samples from
687 elsewhere. Gray shaded circles are samples containing vesicles, from global database (Michael
688 and Graham, 2015), 2011 Axial Seamount eruption (Jones et al., 2018), and Juan de Fuca Ridge
689 (Dixon et al., 1988); white circles are ultradepleted MORB that do not contain vesicles (Michael
690 and Graham, 2015), which likely never reached volatile saturation; black line is 1:1 reference.
691 Samples with vesicles lie mostly above 1:1 reference line, which represents equilibrium
692 degassing due to rapid ascent and emplacement relative to CO_2 degassing timescale (Dixon et al.,
693 1988). Samples from 13°48'N detachment footwall contain vesicles and are undersaturated,
694 which could be explained by post-eruption vertical displacement. Saturation pressures error
695 based on 10% uncertainty in CO_2 and H_2O; collection pressure error for dredged samples
696 obtained from depth at start/end of dredge.
697
698
699
700
701
702 **Figure 7.** Cartoon illustrating hypotheses for near-bottom observations at 13°48'N detachment
703 fault. (a) Initial state: slip on detachment fault accommodates plate spreading prior to
704 deactivation. Gray shaded block is hanging wall, HWC is hanging-wall cutoff; dark gray line is
705 spreading axis; yellow arrows show sediment delivery from water column; yellow shading is
706 sediment cover; black arrow shows slip direction. (b) and (c) Continued slip model: volcanic
707 intrusion (red line/shading) erupts near HWC, followed by continued slip that exposes further
708 footwall on the seafloor. (d) and (e) Late-stage fault model: volcanic intrusion on footwall,
709 causing slip to cease; extension taken up by magmatism in axial valley (pink shading), sediment
710 accumulated on footwall eroded and transported away by current activity (black arrows);
711 volcanic material downthrown by fault (f1) on upper slope of footwall (dashed line).
712
713
714
715

Sample	Lat. (N)	Lon. (W)	Depth (m)	SiO_2 (wt. %)	TiO_2 (wt. %)	Al_2O_3 (wt. %)	FeO (wt. %)	MnO (wt. %)	MgO (wt. %)	CaO (wt. %)	Na_2O (wt. %)	K_2O (wt. %)	P_2O_5 (wt. %)	Total (wt. %)
AL4822-064	13.81817	-44.95136	2767	53.58	1.21	15.38	9.78	0.15	8.27	9.74	2.51	0.08	0.07	100.8
AL4822-065	13.81794	-44.95130	2749	52.98	1.21	15.34	9.74	0.16	8.28	9.71	2.51	0.09	0.07	100.1
AL4822-066	13.81795	-44.95130	2749	52.90	1.21	15.29	9.81	0.16	8.29	9.76	2.50	0.08	0.08	100.1
AL4822-067	13.81636	-44.94960	2731	53.05	1.22	15.39	9.73	0.15	8.19	9.78	2.51	0.09	0.08	100.2

Sample	Lat. (N)	Lon. (W)	Depth (m)	CO_2 (ppm)	H_2O (wt. %)	Saturation Pressure (MPa)	CO_2 vesicles (ppm)
AL4822-064	13.81817	-44.95136	2767	106	0.089	23.1	184
AL4822-065	13.81794	-44.95130	2749	106	0.088	23.2	-
AL4822-066	13.81795	-44.95130	2749	106	0.089	23.2	48
AL4822-067	13.81636	-44.94960	2731	102	0.092	22.3	-

Table 1. Major element compositions, volatile concentrations, and saturation pressures of basaltic samples collected during *Alvin* dive 4822.

Figure 1.

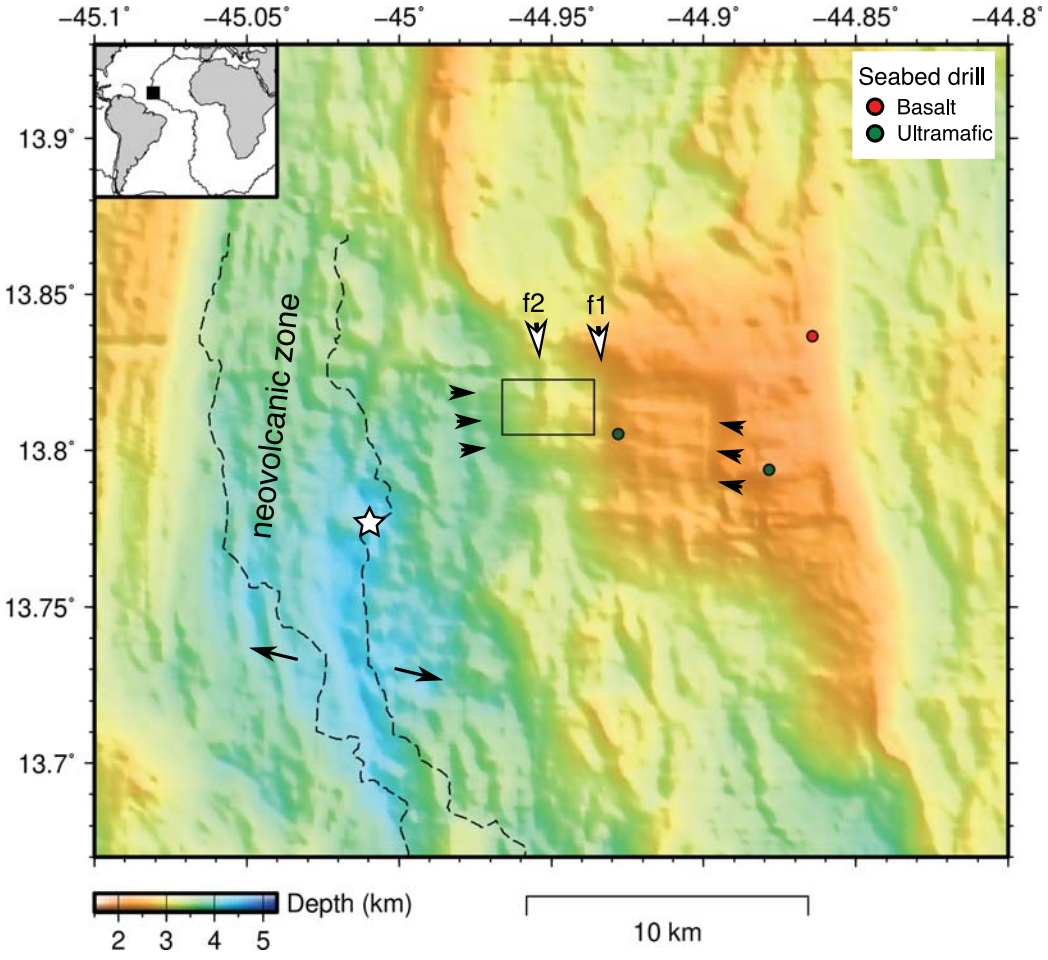
−45.1˚
−45.05˚
−45˚
−44.95˚
−44.9˚
−44.85˚
−44.8˚
13.9˚
13.85˚
13.8˚
13.75˚
13.7˚
Seabed drill
Basalt
Ultramafic
f2
f1
neovolcanic zone
Depth (km)
2
3
4
5
10 km

Figure 2.

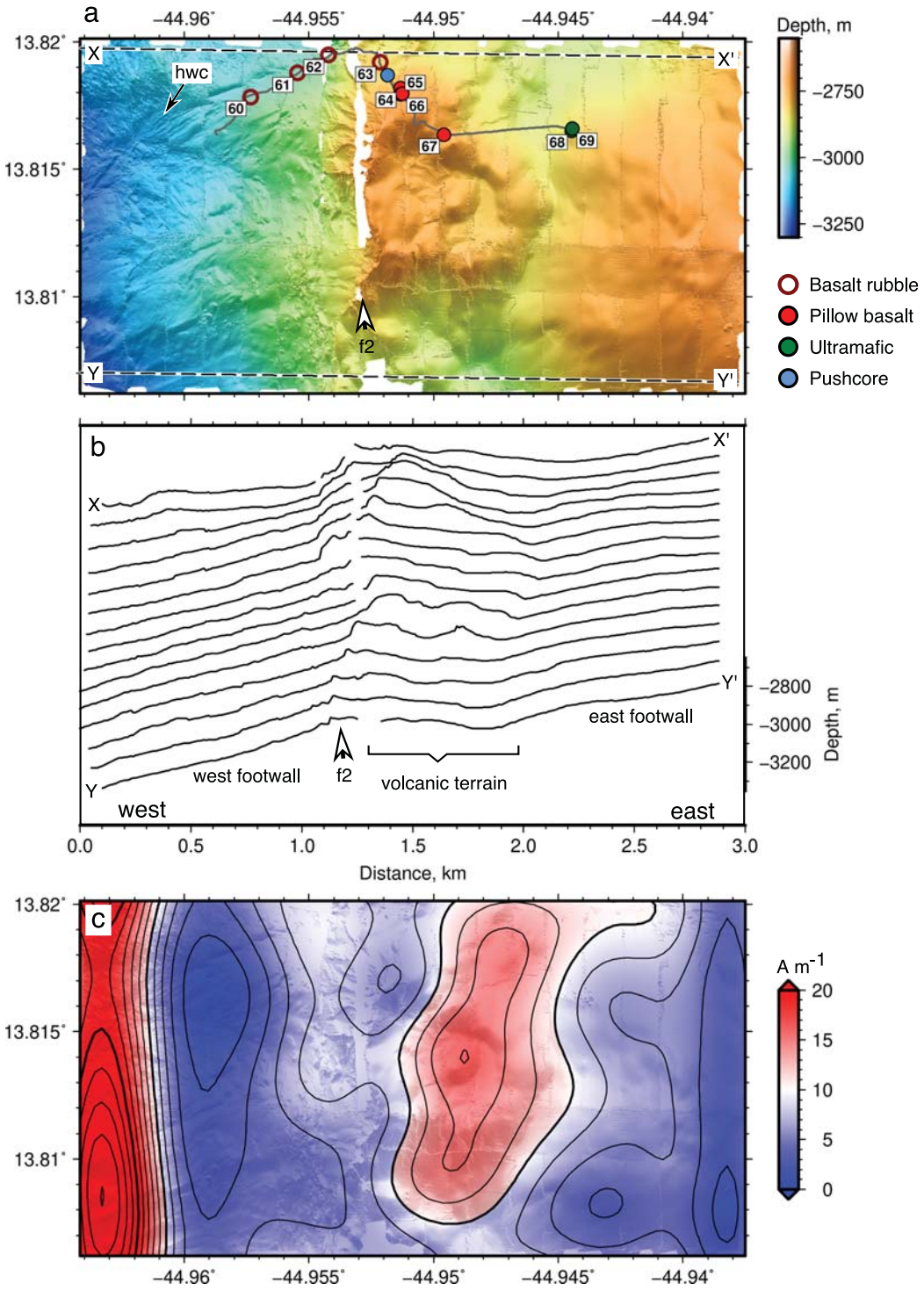
a
−44.96°
−44.955°
−44.95°
−44.945°
−44.94°
13.82°
13.815°
13.81°
X
X'
Y
Y'
hwc
60
61
62
63
64
65
66
67
68
69
f2
Depth, m
−2750
−3000
−3250
Basalt rubble
Pillow basalt
Ultramafic
Pushcore
b
X
X'
Y
Y'
west footwall
f2
volcanic terrain
east footwall
west
east
−2800
−3000
−3200
Depth, m
0.0
0.5
1.0
1.5
2.0
2.5
3.0
Distance, km
c
13.82°
13.815°
13.81°
−44.96°
−44.955°
−44.95°
−44.945°
−44.94°
A m-1
20
15
10
5
0

Figure 3.

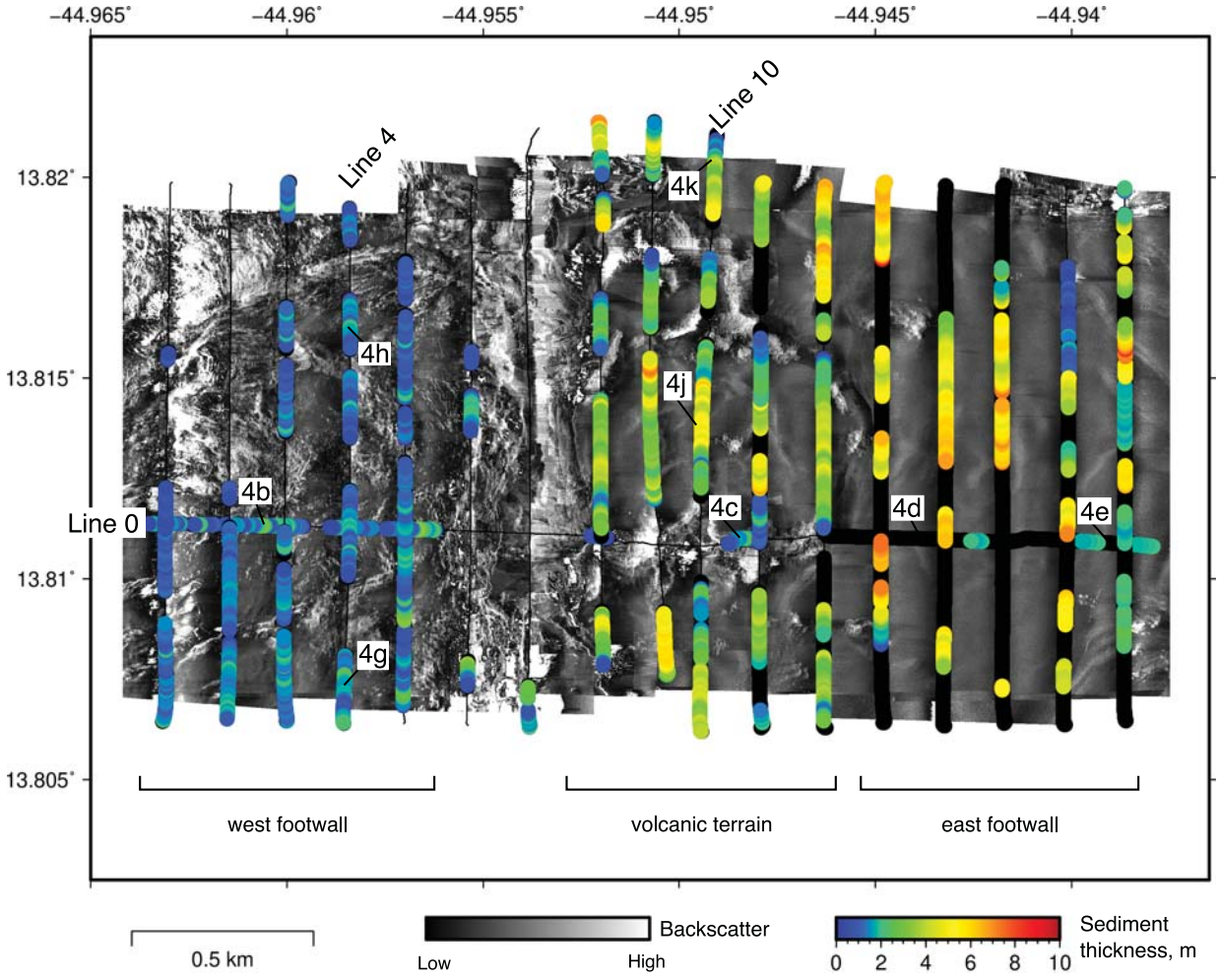
−44.965°
−44.96°
−44.955°
−44.95°
−44.945°
−44.94°
13.82°
13.815°
13.81°
13.805°
Line 4
Line 10
Line 0
4b
4c
4d
4e
4g
4h
4j
4k
west footwall
volcanic terrain
east footwall
0.5 km
Backscatter
Low
High
0
2
4
6
8
10
Sediment thickness, m

Figure 4.

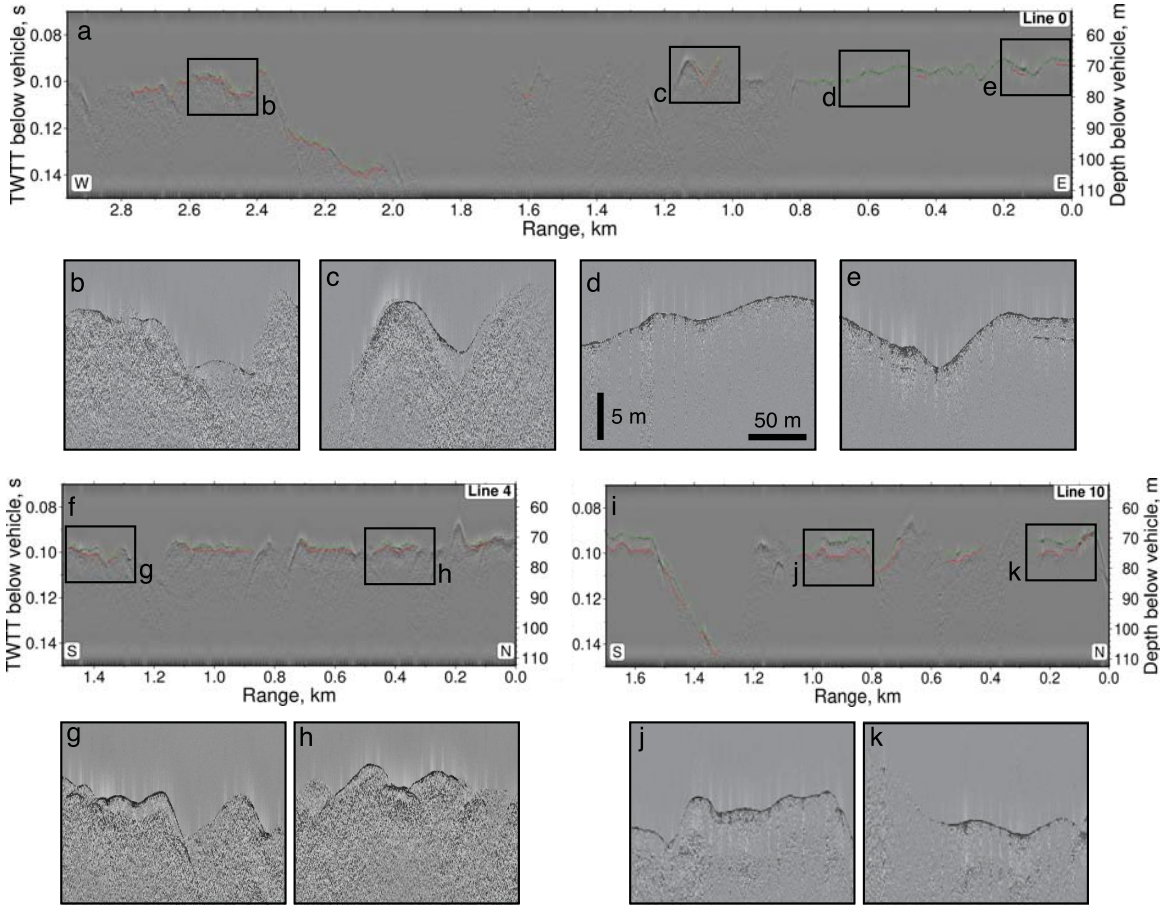
a
Line 0
b
c
d
e
W
E
TWTT below vehicle, s
Depth below vehicle, m
Range, km
5 m
50 m
f
Line 4
g
h
S
N
i
Line 10
j
k

Figure 5.

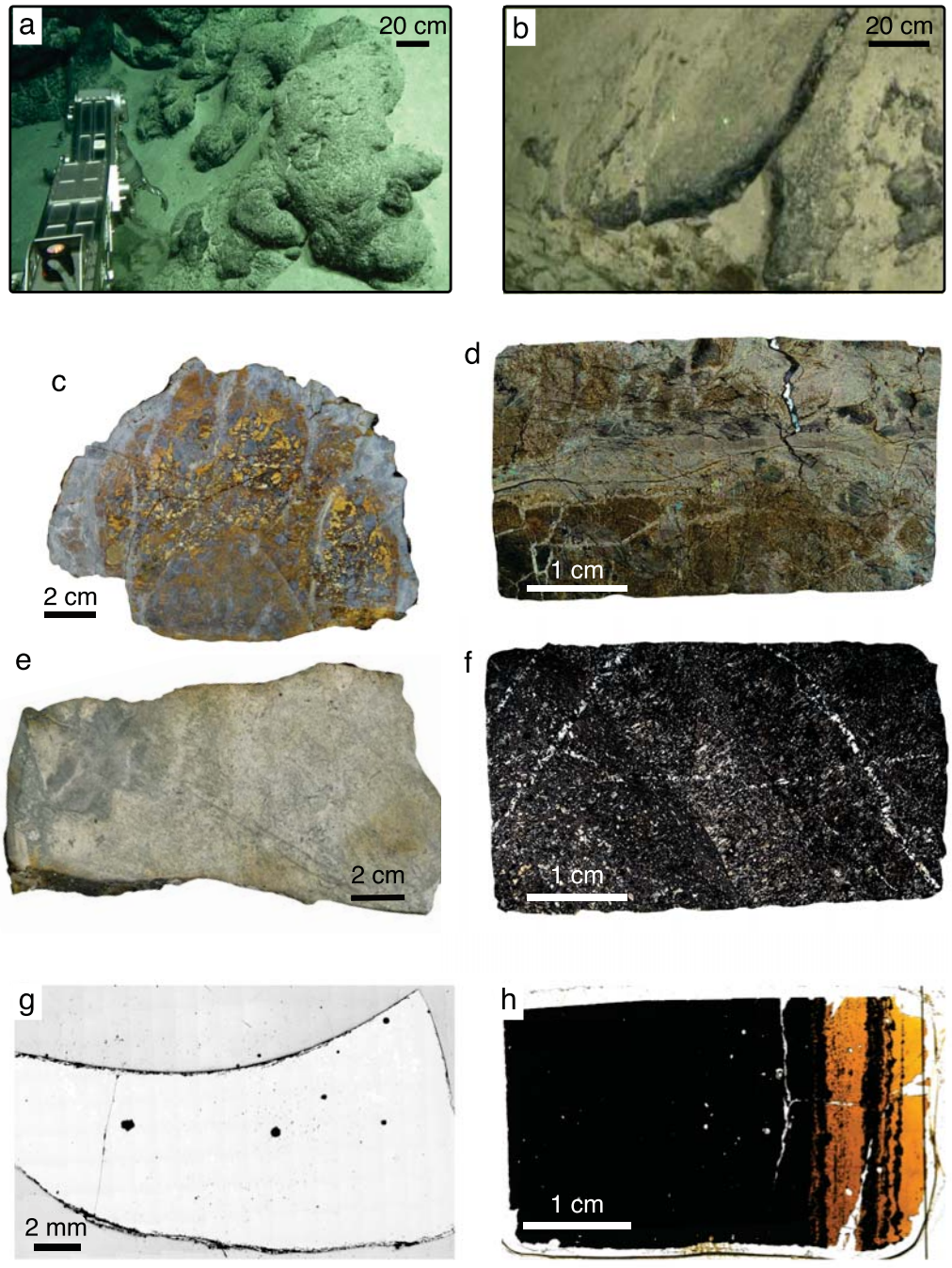
a
20 cm
b
20 cm
c
2 cm
d
1 cm
e
2 cm
f
1 cm
g
2 mm
h
1 cm

Figure 6.

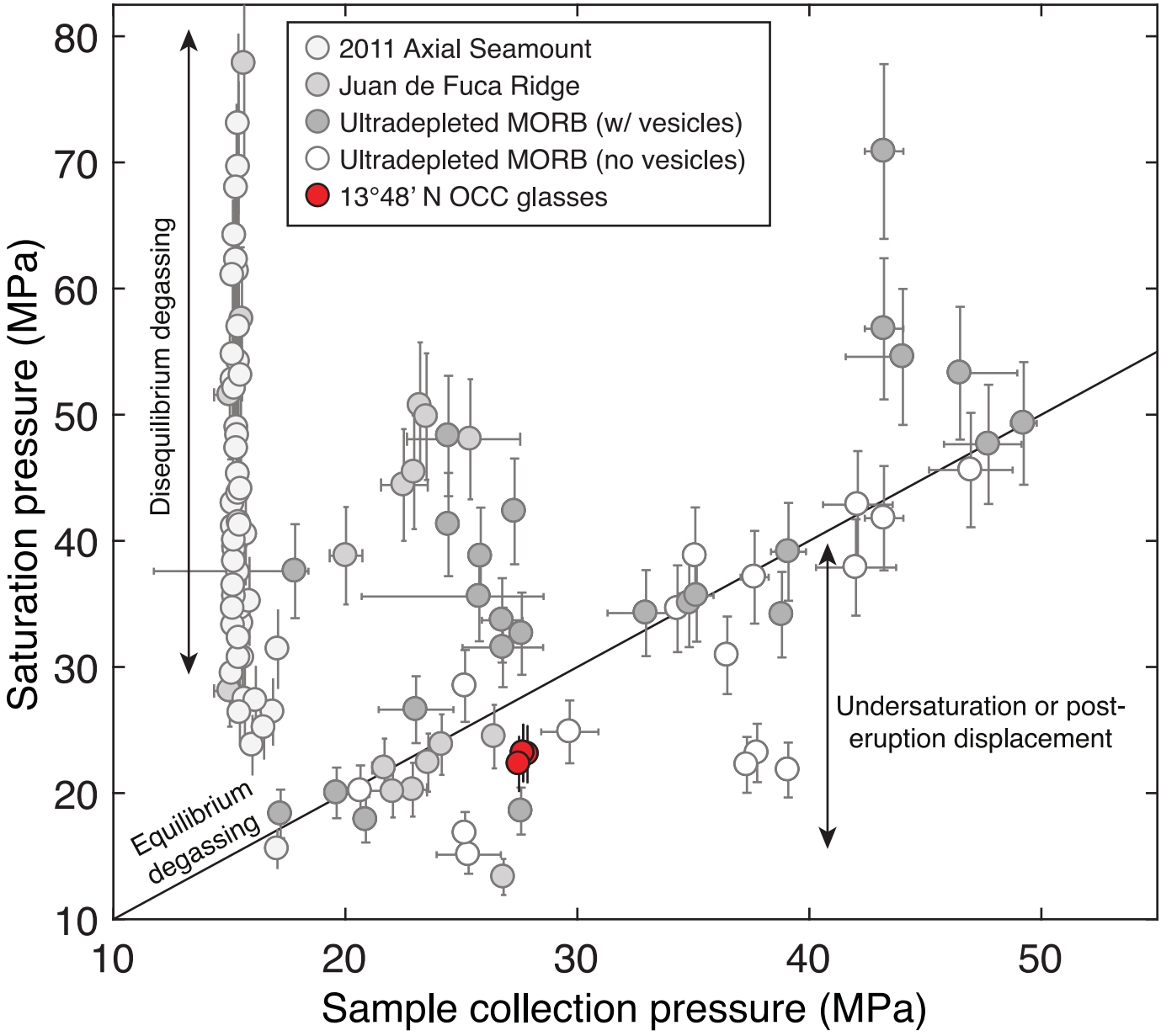
2011 Axial Seamount
Juan de Fuca Ridge
Ultradepleted MORB (w/ vesicles)
Ultradepleted MORB (no vesicles)
13°48' N OCC glasses
Disequilibrium degassing
Equilibrium degassing
Undersaturation or post-eruption displacement
Saturation pressure (MPa)
Sample collection pressure (MPa)
10
20
30
40
50
60
70
80

Figure 7.

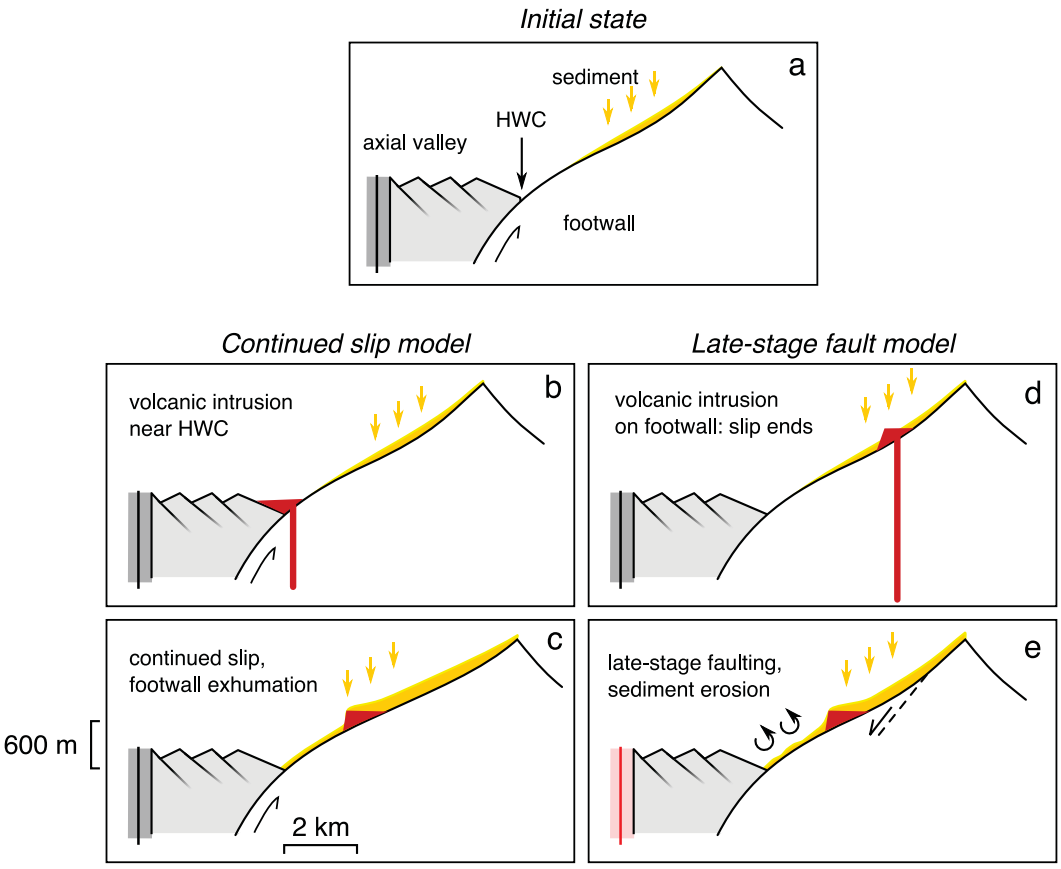
Initial state
a
sediment
HWC
axial valley
footwall
Continued slip model
Late-stage fault model
b
volcanic intrusion
near HWC
d
volcanic intrusion
on footwall: slip ends
c
continued slip,
footwall exhumation
e
late-stage faulting,
sediment erosion
600 m
2 km